

C IV and He II Line Emission of Lyman Alpha Blobs: Powered by Shock Heated Gas

Samuel H. C. Cabot¹, Renyue Cen¹ and Zheng Zheng²

¹*Department of Astrophysical Sciences, Princeton University, Princeton, NJ 08544*

²*University of Utah, Department of Physics and Astronomy, Salt Lake City, UT 84112*

20 October 2018

ABSTRACT

Utilizing *ab initio* ultra-high resolution hydrodynamical simulations, we investigate the properties of the interstellar and circumgalactic medium of Ly α Blobs (LABs) at $z = 3$, focusing on three important emission lines: Ly α 1216Å, He II 1640Å and C IV 1549Å. Their relative strengths provide a powerful probe of the thermodynamic properties of the gas when confronted with observations. By adjusting the dust attenuation effect using one parameter and matching the observed size-luminosity relation of LABs using another parameter, we show that our simulations can reproduce the observed C IV /Ly α and He II /Ly α ratios adequately. This analysis provides the first successful physical model to account for simultaneously the LAB luminosity function, luminosity-size relation, and the C IV /Ly α and He II /Ly α ratios, with only two parameters. The physical underpinning for this model is that, in addition to the stellar component for the Ly α emission, the Ly α and C IV emission lines due to shock heated gas are primarily collisional excitation driven and the He II emission line collisional ionization driven. We find that the density, temperature and metallicity of the gas responsible for each emission line is significantly distinct, in a multi-phase interstellar and circumgalactic medium that is shock-heated primarily by supernovae and secondarily by gravitational accretion of gas.

Key words: methods: numerical, galaxies: clusters: general, galaxies: starburst, quasars: emission lines

1 INTRODUCTION

Ly α blobs (LABs) (e.g., Keel et al. 1999; Steidel et al. 2000; Matsuda et al. 2004) are the largest and most luminous Ly α emitters in the universe, with luminosities of $L_{\text{Ly}\alpha} > 10^{42.5} \text{ ergs s}^{-1}$ and extending up to hundreds of kiloparsecs in size. In the context of galaxy formation, these $z \sim 2-6$ objects are important because they lie in overdense regions, and tend to be proto-galaxy clusters (e.g., Yang et al. 2010; Cen & Zheng 2013). However, the mechanisms which power the Ly α emission of these sources are debated. Cen & Zheng (2013) suggest that central stellar emission (and possibly central AGN) is the primary source of power, with gravitational cooling radiation being the secondary source, in their star-burst model (SBM). The large spatial extent of LABs is a combination of the contribution from clustered sources (galaxies) and spatial diffusion of Ly α photons through resonant scatterings by circumgalactic medium. With detailed radiative transfer calculations, this model is the only model that is able to reproduce both the observed luminosity-size

relation and luminosity function of LABs (Matsuda et al. 2004, 2011).

Recently, Cantalupo et al. (2014) discover one of the largest LABs that contains a luminous quasar, UM 287. In a novel model they propose that the observed Ly α emission could be explained by a high clumping factor ($C \approx 1000$), corresponding to a set of small, cold gas clumps illuminated and photoionized by the quasar. Arrigoni Battaia et al. (2015a) turn to a sample of 13 LABs and explore the possibility that such photoionization is the primary power source of LABs via deep observations of He II and C IV emission lines. Their non-detections of these lines and upper limits on line ratios are reproduced in photoionization models: the optically thin scenario requires $n_{\text{H}} \gtrsim 6 \text{ cm}^{-3}$; the optically thick scenario requires a weak AGN and $N_{\text{H}} > 17.2 \text{ cm}^{-2}$. These results agree with Cantalupo et al. (2014). Arrigoni Battaia et al. (2015b) return to the case of UM 287, seeking to break the degeneracy between clumpiness and the total amount of cool gas (a low clumping factor requires unreasonably high mass for the dark matter halo). Despite extremely deep observations,

they again fail to detect the He II and C IV emission lines. They rule out the optically thick scenario, since it would require too high a Ly α surface brightness (or a covering factor so small that it conflicts with the observed morphology), and thus turn to optically thin models. They find that the Ly α emission is due to dense clumps ($n_{\text{H}} \gtrsim 3\text{cm}^{-3}$) with a radius of $R \lesssim 20$ pc, also in agreement with Cantalupo et al. (2014).

These physical constraints are so strict, however, that it prompts search of alternative models. Indeed, Arrigoni Battaia et al. (2015a) discuss several other candidates for the primary power mechanism, including shocks, gravitational cooling radiation, and resonant scattering (AGN may remain an additional power source, but a non-essential one). Here we use ultra-high resolution simulations to explore the successful starburst model of LABs put forth in Cen & Zheng (2013), where the Ly α emission is primarily powered by central starbursts (and possibly AGN), not due to fluorescence of dense clouds illuminated by quasars. We compute He II and C IV emission of the same LABs analyzed in Cen & Zheng (2013) in addition to the Ly α line. We perform a detailed comparison between the model predictions and extant observational data in Arrigoni Battaia et al. (2015a), Arrigoni Battaia et al. (2015b) and other previous observational studies of LABs (e.g., Dey et al. 2005; Prescott et al. 2009). We find that the He II and C IV emission lines in our model - powered by a combination of both collisional ionization due to shocks and photoionization by resident stars - provide an adequate match to observations with respect to the joint He II / Ly α and C IV / Ly α emission line ratios in the LABs. The success is largely due to the multiphase nature of the CGM in galaxies and a substantial amount of shock heated gas that has favorable temperatures and densities to make large contributions to the line emission in question. It is also relevant to note that an adequate implementation of supernova feedback process is crucial to redistributing metals in the multiphase medium so as to produce the right amount of C IV emission and other metals lines, such as the adequate reproduction of the Si II absorption line width of damped Lyman alpha systems Cen (2012a) and O VI absorption lines in the intergalactic medium Cen (2012b), two exemplary sets of observables spanning a significant range in redshift, gas density, temperature and environment. This paper is structured as follows: In §2 we give description of the simulation and our analysis method. A detailed comparison between simulation results and observational data is in §3. We discuss the physical picture of the emission mechanism in §4. Our conclusions are summarized in §5.

2 SIMULATIONS AND METHODS

2.1 Cosmological Hydrodynamic Simulations

For a more detailed description of the *ab initio* large-scale adaptive mesh-refinement omniscient zoom-in (LAOZI) simulations, performed with the adaptive mesh-refinement (AMR) code, Enzo (Bryan et al. 2014), see Cen (2014). Briefly, we use the WMAP7-normalized (Komatsu et al. 2011) Λ CDM model: $\Omega_M = 0.28$, $\Omega_b = 0.046$, $\Omega_\Lambda = 0.72$, $\sigma_8 = 0.82$, $H_0 = 100h\text{km s}^{-1}\text{Mpc}^{-1} = 70\text{km s}^{-1}\text{Mpc}^{-1}$ and $n = 0.96$. A zoom-in box of size $21 \times 24 \times 20 h^{-3}\text{Mpc}^3$ comoving

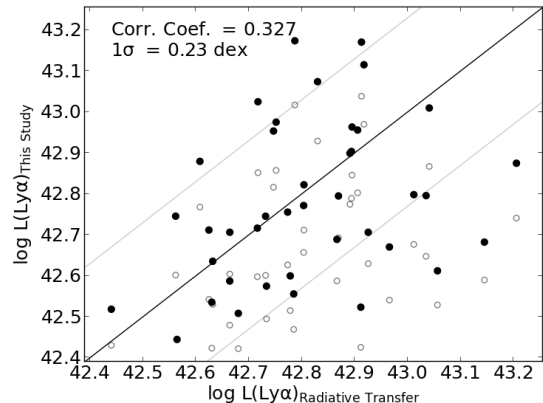


Figure 1. Our Ly α luminosity plotted against that obtained from detailed radiative transfer. 1σ deviation lines are plotted surrounding the equality line. The parameter value $\gamma = 6$ is used to generate our values shown here (filled points). For comparison, we also show the poor scatter and downward shift generated by $\gamma = 7.5$ (open points).

is embedded in a $120 h^{-1}\text{Mpc}$ periodic box. The maximum resolution in the zoom-in box is better than $111 h^{-1}\text{pc}$ (physical) at all times. Star formation follows the prescription of Cen & Ostriker (1992). Supernova feedback from star formation is modeled following Cen et al. (2005). The Haardt & Madau (2012) UV radiation background is used in the simulation along with a treatment of self-shielding Cen et al. (2005). This is the same simulation used in the successful demonstration of a starburst based model for the LABs (Cen & Zheng 2013), coupled with detailed radiative transfer calculations of Ly α radiation and the successful interpretation of the observed diffuse Lyman-alpha halos in Lyman-alpha emitting galaxies (Lake et al. 2015). Since the goal of the simulations is to model shock flows, AGN feedback is not included (though could be added).

Shock velocities are due to gravitational interactions and stellar feedback, and velocities range from about 100km s^{-1} to 1000km s^{-1} . If the shock velocities are too high or too low for a given species, that particular shock would not contribute much; the abundant species are shocked to the correct temperatures by shocks of appropriate velocities. These velocities cover both the low velocity outflows observed by (Yang et al. 2014), and accommodate large-scale outflows caused by strong shocks as predicted by Taniguchi & Shioya (2000) and Mori & Umemura (2006); they are also consistent with the velocities from the shock model in Arrigoni Battaia et al. (2015a) that explain the observed line ratios ($> 250\text{km s}^{-1}$). While 1000km s^{-1} outflows are not excluded from our model, we expect line emission to be primarily dominated by internal shock heated gas, driven by both supernova feedback and gravitational accretion. These processes may explain the observational bias of lower velocities (Yang et al. 2011, 2014) and are consistent with the findings of McLinden et al. (2013).

2.2 Analysis Method

Our analysis method consists of three steps. First, we utilize the spectral synthesis code Cloudy version 13.03 (Fer-

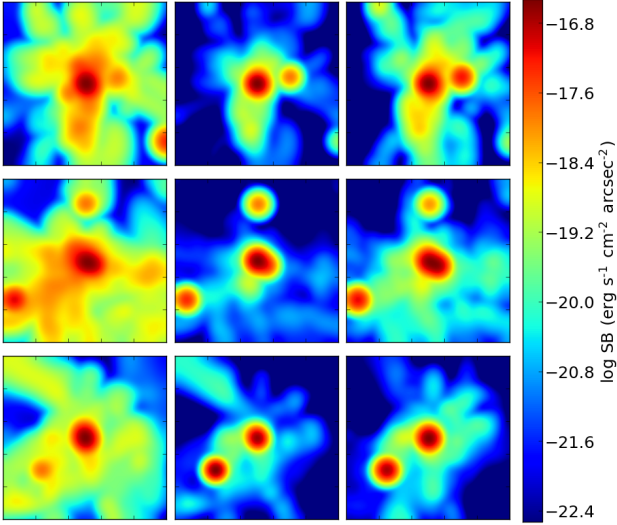


Figure 2. Surface brightness maps of size $100 \times 100 \text{ kpc}^2$ for three randomly selected galaxies with ID: 0 (top row), 20 (center row), and 42 (bottom row), projected along a depth of 100 kpc. The maps are in each emission wavelength: Ly α (left column), He II (center column) and C IV (right column). A gaussian blur of full width at half maximum (FWHM) = 1'' was applied to the images to simulate seeing conditions in Cantalupo et al. (2014) (FWHM = 0.6 - 1.0'') and Arrigoni Battaia et al. (2015a) (0.5 - 1.4'').

land et al. 2013) to generate emission spectra (the transmitted continuum component, in Cloudy) over a range of gas density and temperature at solar metallicity. Line emissions for Ly α , C IV and He II are tabulated for a two-dimensional grid spanning density $n_H = 10^{-4} - 10^4 \text{ cm}^{-3}$ and temperature $T = 10^3 - 10^6 \text{ K}$, both with steps of 0.025 dex. We use the Haardt & Madau (2012) UV background incident radiation field at $z = 3.1$ for the calculation, subject to self-shielding effect of each individual region based on local optical depth calculations.

Second, we select 40 most massive galaxies in our simulation at $z = 3.1$, the same sample used in the LAB model paper (Cen & Zheng 2013). We then use the analysis software yt version 2.6 (Turk et al. 2011) to perform the following for each galaxy:

(i) We identify a cubic region of length 100 kpc centered on the galaxy, which covers approximately the area of the $2.2 \times 10^{-18} \text{ erg s}^{-1} \text{ cm}^{-2} \text{ arcsec}^{-2}$ Ly α isophotal region in Arrigoni Battaia et al. (2015a), and Matsuda et al. (2004).

(ii) We obtain physical variables, including density, temperature, metallicity, and self-shielding optical depth on a unigrid covering the 100 kpc cube at the resolution of 160 pc. The HM background is subject to self-shielding attenuation, and is computed as $\varepsilon = \varepsilon_0 \times \langle \exp(-n_H h \sigma_\lambda) \rangle_{\text{cell}}$, where ε_0 is unattenuated emission, n_H is the neutral hydrogen density of the cell, h is the local scale-height along each of the six faces of the cell and σ_λ is the mean absorption cross section of ionizing photons given the spectral shape of the HM background. The attenuation average " $\langle \rangle_{\text{cell}}$ " is done over the six faces of the cell.

(iii) We use the Cloudy generated emissivity lookup tables to obtain line emissions for each grid cell (of size 160 pc)

within the 100 kpc box. The metallicity parameter is a multiplicative factor since our table depends only on temperature and density with the assumed solar metallicity.

(iv) We add the stellar contribution to the Ly α emission in each grid cell, and use a scaling relation that a star formation rate (SFR) of $1 \text{ M}_\odot/\text{yr}$ produces $L_{\text{Ly}\alpha} = 1 \times 10^{42} \text{ erg s}^{-1}$ (Zheng et al. 2010; Cen & Zheng 2013).

(v) We model dust obscuration for the emission as follows (this is for dust on small scales within the galaxies; while there may be dust on $\sim 100 \text{ kpc}$ scales (e.g., Peeples et al. 2014), we do not assume so). The optical depth at wavelength λ along each of the six faces of each grid cell is

$$\tau_\lambda = 0.49 \times \frac{Z}{Z_\odot} \frac{N_H}{10^{21}} \frac{A_\lambda}{A_v} \beta (1 + \gamma) \quad (1)$$

where $A_v = 4.89 \times 10^{-22}$ and A_λ is the absorption coefficient at the emission line wavelength (Draine 2003), Z is gas metallicity of the cell, β is to account for the uncertainties in metal (hence dust) density modeling uncertainty in the simulation and γ is zero for non-resonant lines (He II) and nonzero to account for scatterings of resonant lines (Ly α and C IV). In our case, to be self-consistent, a single γ applies to both Ly α and C IV lines. Note that we only have two free parameters in our calculations, with four outputs - Ly α luminosity, Ly α luminosity-size relation, C IV / Ly α ratio and He II / Ly α ratio. The metallicity-weighted column density N_H is determined by computing the scale-height of the metallicity-weighted neutral hydrogen (volumetric) density along each of the six faces of each grid cell, then multiplied by the hydrogen volumetric density of the cell. This is done using a smoothed covering grid, which interpolates coarse regions of the simulation to match high resolution dimensions. The mean transmitted emission $\langle L \rangle$ for each emission line from each grid cell is computed using

$$\langle L \rangle = L < e^{-\tau_\lambda} \rangle, \quad (2)$$

averaged over six faces of each grid cell, where L is the intrinsic line emission, including contribution from both shock heated gas and stars.

Let us now discuss the purpose and logic of having two parameters, β and γ (Eq 1). We first note that we have three separate emission lines and only two free parameters in our calculation. Since we do not perform detailed, expensive radiative transfer calculations for the C IV line that is a resonant line, we use the parameter γ in Eq 1 as a proxy method, in the following sense. The parameter γ (or more precisely, $\beta(1 + \gamma)$) is adjusted to reproduce, within the scatter, the Ly α emission obtained through detailed radiative transfer calculations performed in Cen & Zheng (2013). We use the same γ for the C IV line. That leaves us with only one free parameter β that we vary, admittedly by hand, with the sole purpose of searching for a match to the observations in the He II / Ly α - C IV / Ly α line ratios plane. Since the observable numbers outnumber the adjustable parameters here, a successful outcome from this "fitting" exercise represents a non-trivial result. It is noted, though, that if the C IV emission is lower than required to yield reasonable fit, there would be no adequate match to observations.

We find that parameters within $\pm \sim 25\%$ of $\beta = 2/7$ and $\gamma = 6$ are able to provide a reasonable match to observations with respect to the C IV / Ly α ratio and He II / Ly α ratio, as well as being able to reproduce Ly α luminosities of galaxies

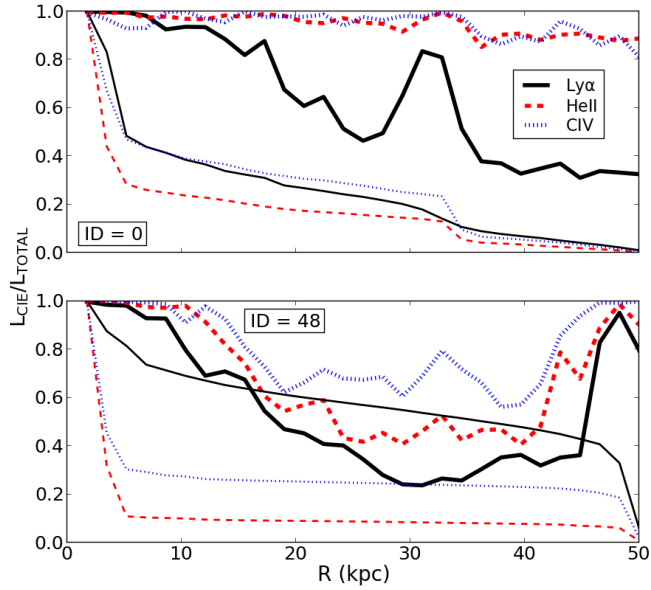


Figure 3. Radial profiles of the fractional luminosity produced by collisional processes for Ly α (solid black line), He II (dashed red line), and C IV (dotted blue line). Thick lines represent the differential profile, and thin lines are the normalized cumulative total luminosity. The latter demonstrate that most of the emission is concentrated in the central regions. The panels represent galaxies of two very different stellar mass regimes: $4.33 \times 10^{11} M_{\odot}$ (Top) and $5.43 \times 10^{10} M_{\odot}$ (Bottom).

obtained with detailed Ly α radiative calculations (Cen & Zheng 2013). The correlation between our Ly α emission and that from radiative transfer is shown in Figure 1. Also shown is the case of $\gamma = 7.5$. We determine our eventual value of γ such that the scatter is minimized. We find that the 1σ r.m.s variation is ~ 0.2 dex in L_{τ}/L_{RT} , where L_{τ} and L_{RT} are the Ly α luminosity computed here and that computed using radiative calculations (Cen & Zheng 2013), respectively; the r.m.s. variation is consistent with and within the variation among different viewing angles for a typical galaxy with detailed radiative transfer calculations (Zheng & Wallace 2014). In any case, this small variation does not alter our conclusions reached below. However, small variations of 10 – 30% on either of the two parameters (β and γ) change the results significantly, and in some cases may render the results inconsistent with observations.

In Figure 2 we show surface brightness maps for three randomly selected galaxies. Overall, the emissions for all three lines follow the galactic structure centered on the galaxy. In finer details, they display significant differences, which are ultimately due to the fact that the regions that are responsible for three emission lines are different, arising from regions of different physical characteristics in a multi-phase medium, as will be made clear later. Table 1 summarizes the luminosities of the three lines and two ratios for each of the 40 galaxies in the simulation. Contribution from collisional processes is easily separated from the UV photoionization/photoexcitation component by setting the ionization parameter to 0 for all of the simulation space. We find that emission from collisional processes traces the total emission (shown for a few galaxies in Figure 2), and accounts for the vast majority ($> 70\%$) of the total lumi-

nosity for each line in Table 1, indicating that the photoionization/photoexcitation contribution is small. The fractional luminosity produced by collisional processes is depicted in Figure 3. It is clear that the collisional processes are largely responsible for the emission in the central region that dominates the overall emission. In the outer regions, however, the photoionization/excitation processes make a significant, sometimes larger, contribution. Note that the ratios reported here are derived from emission over the entire 100kpc box, with no surface brightness threshold. Because our emission model does not use radiative transfer, we are unable to produce isophotes or sizes of the LABs. However, in the next section we discuss an approach to approximate effects of SB thresholds using previous radiative transfer data, which allows fair comparisons to observations.

3 COMPARISON BETWEEN SIMULATION RESULTS AND OBSERVATIONS

We now turn to a detailed, statistical comparison of our simulation results with extant observations. As noted in Arrigoni Battaia et al. (2015a), much of the available literature on LABs and similar objects report different imaging techniques (e.g. slit or 2-dimensional) and of different regions (e.g. extended emission or core). Thus it is useful to bear in mind the heterogeneity in assessing the comparison results.

In the deepest He II and C IV narrow-band images ever taken, Arrigoni Battaia et al. (2015a) fail to detect He II or C IV emission above the 1σ surface brightness (SB) detection limit of 4.2×10^{-19} and 6.8×10^{-19} ergs s $^{-1}$ cm $^{-2}$ arcsec $^{-2}$, respectively, in two-dimensional images of 13 LABs. They are able to place upper limits on the ratios of these two lines to Ly α , with the strongest constraints of He II / Ly α < 0.11 and C IV / Ly α < 0.16 due to the two LABs with the largest isophotal area. The 2σ SB threshold for Ly α is 2.2×10^{-18} ergs s $^{-1}$ cm $^{-2}$ arcsec $^{-2}$ (Matsuda et al. 2004). Prescott et al. (2009) obtain slit spectra of the emission lines with a 1σ detection limit of $\sim 10^{-17}$ ergs s $^{-1}$ cm $^{-2}$ arcsec $^{-2}$, and determine line ratios for He II / Ly α and C IV / Ly α from observations of a giant Ly α nebula (PRG1). Prescott et al. (2013) study two other nebulae (PRG2, PRG3) with 1σ detection threshold of $\sim 10^{-18}$ ergs s $^{-1}$ cm $^{-2}$ arcsec $^{-2}$. Dey et al. (2005) also performed observations of a LAB with a SB detection limit of $\sim 10^{-18}$ ergs s $^{-1}$ cm $^{-2}$ arcsec $^{-2}$. Heckman et al. (1991b) perform analysis of slit spectra of several radio-loud quasars (QSRs), which have similar properties compared to LABs with respect to size and extent of the Ly α emission. The detection limit of the observations was approximately 3.0×10^{-17} ergs s $^{-1}$ cm $^{-2}$ arcsec $^{-2}$ (Heckman et al. 1991a) and they obtain upper limits on the emission line ratios.

In order to place the observational results detected with varying surface brightness detection limits, we have adjusted all observed data to the Ly α surface brightness threshold 2.2×10^{-18} ergs s $^{-1}$ cm $^{-2}$ arcsec $^{-2}$ of Matsuda et al. (2004). This adjustment process is calibrated as follows: We use radiative transfer calculations for the galaxies in our sample (listed in Table 1), which allows us to compute ratios of fluxes of the Ly α line at any two imposed surface brightness thresholds. We then average over the 40 galaxies to obtain the mean of the appropriate ratio in question between two adopted surface brightness thresholds. Since our calculations of three

Table 1. Star formation rate, stellar mass, halo mass and luminosities over the 100kpc cube for each galaxy in our sample, and the corresponding ratios. Also emission-weighted metallicity, density and temperature. Column 2 [$M_{\odot} \text{ yr}^{-1}$], Column 3-4 [$10^{10} M_{\odot}$], Column 5-8 [$10^{42} \text{ ergs s}^{-1}$] Column 11-13 [Z_{\odot}], Column 14-16 [cm^{-3}], Column 17-19 [10^4 K].

ID	SFR	M*	M _{Halo}	L _{Lyα}	L _{Lyα} *	L _{HeII}	L _{CIV}	HeII Ly α	CIV Ly α	(Z) (Ly α)	(Z) (HeII)	(Z) (CIV)	(n _H) (Ly α)	(n _H) (HeII)	(n _H) (CIV)	(T) (Ly α)	(T) (HeII)	(T) (CIV)
0	409.20	43.31	397.7	11.825	5.457	0.094	0.407	0.008	0.034	0.55	0.80	0.79	3.04	14.58	2.90	2.45	24.93	11.30
1	129.60	36.78	234.7	6.218	1.293	0.114	0.745	0.018	0.120	0.40	1.10	1.15	3.12	7.21	3.66	2.77	18.92	11.05
2	105.40	35.57	231.4	7.565	4.444	0.075	0.970	0.010	0.128	0.71	1.46	1.58	1.20	6.47	2.52	2.39	11.59	10.65
3	113.80	29.26	192.2	10.576	4.297	0.175	0.744	0.017	0.070	0.48	0.78	0.66	6.30	15.87	5.53	2.51	13.13	10.44
4	86.58	27.08	334.6	13.028	2.019	0.167	1.775	0.013	0.136	0.46	0.92	0.93	3.02	7.36	4.05	2.07	10.66	10.40
5	75.82	22.57	194.4	7.922	4.083	0.038	0.371	0.005	0.047	0.61	1.04	1.16	1.59	4.90	2.56	2.28	12.68	10.57
6	87.79	20.33	175.2	14.800	5.441	0.115	1.155	0.008	0.078	0.54	1.00	1.11	2.29	5.53	2.69	2.03	9.71	10.58
7	86.42	19.25	148.0	4.879	2.226	0.041	0.399	0.008	0.082	0.55	1.25	1.09	1.74	9.93	2.82	2.37	15.64	11.09
8	100.20	18.31	141.0	5.080	2.204	0.056	0.204	0.011	0.040	0.46	1.30	1.09	0.70	13.53	2.51	2.22	12.82	11.24
9	38.50	17.13	137.7	6.638	2.071	0.071	0.541	0.011	0.081	0.47	1.05	1.07	2.20	6.99	3.69	2.30	9.44	10.43
11	62.07	16.69	100.1	5.906	2.117	0.055	0.802	0.009	0.136	0.72	1.17	1.22	1.98	5.63	2.92	2.36	9.41	10.75
12	106.30	16.59	124.8	14.914	6.686	0.137	1.011	0.009	0.068	0.62	1.00	0.99	3.75	9.08	4.33	2.08	9.13	10.52
14	71.34	15.13	139.6	9.184	3.426	0.129	0.803	0.014	0.087	0.48	1.29	1.15	2.41	12.44	4.31	2.10	9.70	10.51
15	57.44	14.06	117.9	9.439	3.198	0.041	0.240	0.004	0.025	0.44	0.97	0.83	1.60	9.43	2.73	1.92	10.40	10.51
16	74.77	13.92	137.9	5.142	2.100	0.119	1.261	0.023	0.245	0.76	1.11	1.11	3.86	7.75	4.00	2.46	9.68	10.75
19	37.27	12.73	115.9	8.978	1.933	0.042	0.269	0.005	0.030	0.50	1.08	0.76	1.73	12.43	2.15	2.00	10.45	10.47
20	84.87	12.67	167.3	6.276	1.779	0.130	0.433	0.021	0.069	0.49	1.08	0.99	1.36	16.15	3.99	2.16	11.24	10.88
21	44.42	12.16	100.5	5.562	1.441	0.047	0.321	0.009	0.058	0.40	1.01	0.98	3.24	8.55	3.40	2.11	9.51	10.54
23	79.97	10.54	98.6	4.808	0.722	0.044	0.233	0.009	0.048	0.42	1.64	1.58	0.52	10.36	3.38	1.94	9.65	10.61
25	22.56	9.17	196.3	8.004	1.023	0.081	0.544	0.010	0.068	0.42	1.38	1.13	1.53	10.18	2.96	1.92	10.38	10.86
26	67.92	7.76	87.1	3.593	1.017	0.040	0.178	0.011	0.050	0.41	1.69	1.41	0.57	14.46	3.14	2.00	12.89	10.65
28	43.67	7.54	80.4	5.201	1.298	0.059	0.653	0.011	0.125	0.49	1.04	1.03	2.01	6.10	4.05	2.36	9.11	10.29
29	12.67	7.62	53.9	5.563	0.635	0.251	0.304	0.045	0.055	0.28	0.37	0.53	5.01	48.90	17.82	1.86	8.94	10.84
30	31.54	7.42	94.8	10.221	1.295	0.029	0.342	0.003	0.033	0.52	0.78	0.96	1.92	3.61	2.02	1.96	8.20	10.49
31	14.15	7.57	61.3	3.297	0.619	0.006	0.036	0.002	0.011	0.38	0.40	0.52	0.98	1.24	0.45	2.23	13.74	10.79
32	26.54	7.32	73.3	9.030	2.660	0.064	0.614	0.007	0.068	0.44	0.93	0.83	4.37	6.15	3.00	2.15	8.30	10.22
33	16.78	7.02	44.0	3.222	0.785	0.018	0.114	0.005	0.035	0.35	1.38	1.39	0.78	8.31	2.41	2.20	9.95	10.66
34	25.14	6.94	102.6	6.234	0.949	0.016	0.203	0.003	0.033	0.39	0.95	1.17	0.89	3.10	2.14	1.88	9.66	10.68
35	8.44	6.74	63.5	3.755	0.513	0.005	0.043	0.001	0.011	0.42	0.50	0.80	0.51	0.61	0.41	1.88	8.25	9.94
37	18.92	6.65	149.3	5.082	0.638	0.059	0.250	0.012	0.049	0.55	1.44	1.14	0.92	12.80	3.04	1.96	10.64	11.02
38	18.09	6.57	104.0	4.092	0.996	0.039	0.179	0.009	0.044	0.48	1.70	1.30	0.70	14.47	3.37	2.04	11.29	10.78
40	24.14	6.50	109.0	7.492	1.231	0.057	0.381	0.008	0.051	0.50	1.12	1.10	1.77	9.15	2.82	1.96	10.03	10.78
41	7.26	6.38	49.2	2.782	0.566	0.006	0.068	0.002	0.024	0.35	1.43	1.75	0.97	3.12	2.04	1.93	8.58	10.37
42	17.91	6.09	57.7	3.864	0.718	0.013	0.108	0.003	0.028	0.41	1.01	1.12	1.17	3.83	3.00	2.13	9.16	10.56
43	23.99	5.78	43.7	3.429	0.462	0.049	0.190	0.014	0.055	0.37	1.32	1.08	0.97	16.71	3.69	1.91	10.82	11.50
44	66.83	5.81	62.7	5.691	2.199	0.115	1.082	0.020	0.190	0.56	0.98	1.04	3.02	7.74	4.46	2.38	9.00	10.73
45	37.83	5.90	52.4	4.678	1.390	0.053	0.263	0.011	0.056	0.46	1.04	1.01	2.11	10.70	4.14	2.26	9.62	10.82
46	26.04	5.55	47.4	3.977	2.036	0.020	0.080	0.005	0.020	0.44	1.70	1.52	0.66	9.18	3.35	2.10	10.70	10.70
47	24.20	5.39	57.2	3.335	0.370	0.040	0.291	0.012	0.087	0.36	1.77	1.48	1.24	12.18	3.40	2.01	10.47	10.72
48	46.03	5.43	126.0	4.318	0.954	0.054	0.232	0.012	0.054	0.61	1.46	1.16	1.11	13.35	3.12	1.97	10.76	10.97

lines here do not involve detailed radiative transfer, which are important for both Ly α and C IV lines, we also apply the same adjustments to the simulated galaxies, but on an individual galaxy basis. The adjustment consists of multiplying the He II /Ly α emission line ratios by a ratio of L_{Ly α} values at the observed and desired surface brightness thresholds. We do not apply this adjustment to C IV /Ly α since their emissions track each other. We choose our method of calibrating various observations of varying SB thresholds to a common one, because it allows us to place all data, observational or theoretical, on the same plot, instead of making comparisons between simulation and each observational data set on separate plots. Given the relatively small sample size, this is preferred also for making statistical tests, such as the KS test we perform.

Figure 4 shows a quantitative comparison between our simulation results and observations. First, it is evident that

the upper limits by Arrigoni Battaia et al. (2015a) are visually consistent with our simulation results in that the bulk of the simulated results are below the upper limits in both x and y axes. There is no significant dependence on mass, except perhaps that lower mass galaxies represent the smallest ratios, as shown by the predominantly blue diamonds in the lower left corner of Figure 4. Second, a comparison between our simulations results and the observed detections (not counting the upper limits), using a two-sample Kolmogorov-Smirnov test, yields a p-value of 0.24 for the He II /Ly α ratio data and 0.13 for the C IV /Ly α ratio data. These two KS p-values, if treated as independent, would give a combined KS p-value ($= p_1 p_2 [1 - \ln(p_1 p_2)]$) of 0.14, which indicates an acceptable match. We find that we could adjust the parameter β in Eq 1 down somewhat to significantly increase the KS test p-value for the He II /Ly α ratio; the KS test p-value for the C IV /Ly α ratio has not been

optimized either. This is because we feel that such an exercise is not necessarily the most meaningful and may lead to a misperception of too good agreement between simulations and observations. Such an exercise will become useful, only when the number of observational detections increases by an order of magnitude. In short, our simulation results with two parameters provide, for the first time, a successful model to reproduce the two line emission ratio $\text{He II}/\text{Ly}\alpha$ and $\text{C IV}/\text{Ly}\alpha$ in LABs, in addition to simultaneously reproducing the $\text{Ly}\alpha$ luminosity function and luminosity-size relation, as shown earlier in [Cen & Zheng \(2013\)](#).

4 UNDERLYING PHYSICS IN OUR MODEL FOR THE EMISSION LINES

The combination of mass budget constraint and required high $\text{Ly}\alpha$ luminosity place strong physical constraints on volumetric density, column density and size of the gas in the extended region around the quasar UM287 observed in the photoionization fluorescence model of [Arrighi Battaia et al. \(2015b\)](#): $n_{\text{H}} \gtrsim 3 \text{ cm}^{-3}$, $N_{\text{H}} \lesssim 10^{20} \text{ cm}^{-2}$, and gas clumps with $R \lesssim 20 \text{ pc}$. They find that, unless the metallicity of the line emitting dense gas is very low ($\lesssim 0.001 Z_{\odot}$), the expected $\text{He II}/\text{Ly}\alpha$ ratio values obtained in their model reside above the strongest upper limits (the left-most green plus in Figure 4). Higher metallicities ($0.1 - 1.0 Z_{\odot}$) are permitted by only if $\log(n_{\text{H}}/\text{cm}^{-3}) \sim 1.5$. While not direct proof of the relatively high metallicity for the He II emitting gas, we find in the simulation that the emission-weighted metallicity of the He II emitting gas is $\sim 1.1 Z_{\odot}$, ranging from $0.37 - 1.77 Z_{\odot}$. Even though some galaxies have a very high emission-weighted density, the majority of our sample is below 10 cm^{-3} .

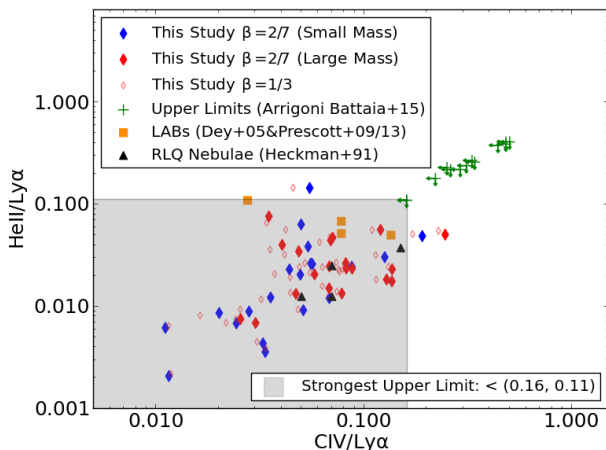


Figure 4. Comparison of the model line ratios (blue and red diamonds) with observations. Blue and red divide our galaxy sample into two halves, lower ($5.39 \times 10^{10} - 7.76 \times 10^{10} M_{\odot}$) and upper ($9.17 \times 10^{10} - 4.33 \times 10^{11} M_{\odot}$) stellar mass bins respectively. For comparison, we also plot ratios from a varied β (red open diamonds). The observational data are detections from [Heckman et al. \(1991b\)](#) (solid black triangles) of several radio-loud quasars, from [Dey et al. \(2005\)](#), [Prescott et al. \(2009\)](#) and [Prescott et al. \(2013\)](#) (solid orange squares) of LABs, and upper limits from [Arrighi Battaia et al. \(2015a\)](#) (green pluses with arrows), with the strongest upper limits shown as the grayed shaded region.

Our model is based on *ab initio* ultra-high resolution cosmological hydrodynamical simulations and takes into account all possible emission processes. This includes gravitational shocks due to collapse of structures (galaxies within proto-clusters) and feedback shocks due to supernova explosions, which are both energetically important, in addition to photoionization by stars. Although an additional component of radiation from the central AGN may be included, we do not do so in this analysis and, as we have shown, it is not necessarily needed or beneficial in terms of providing a good model matching observations.

The physical characteristics of the emission regions in our model are shown in Figure 5. The emission of each of the three lines (left panel for $\text{Ly}\alpha$, middle panel for He II and right panel for C IV) in the temperature-density phase diagram is shown in the top row, whereas the distributions of each emission line in density (left panel) and temperature (right panel) for $\text{Ly}\alpha$, He II and C IV lines are shown in black solid, red dashed and blue dotted curves, respectively, in the bottom row. We see in Figure 5 that most of the $\text{Ly}\alpha$ emission originates from the gas with $\log(n_{\text{H}}/\text{cm}^{-3}) = 0 - 1$ and $\log(T/\text{K}) \sim 4.2$. Since $\text{Ly}\alpha$ is a resonant line, the most efficient (and economical) powering mechanism via collisions is normally collisional excitation, instead of collisional ionization. Thus, a most noteworthy fact is the temperature of $10^{4.2} \text{ K}$ for the $\text{Ly}\alpha$ emitting gas, which is the optimal temperature for $\text{Ly}\alpha$ line emission via excitation, where the fractions of neutral and ionized hydrogen are roughly comparable. It is thus clear that collisional excitation (rather than collisional ionization) by combined gravitational and feedback shocks is a major source of $\text{Ly}\alpha$ emission. From the cooling point of view, this indicates that $\text{Ly}\alpha$ line emission is a significant cooling mechanism for shock heated gas. The metallicity ($\sim 0.5 Z_{\odot}$) of the $\text{Ly}\alpha$ emitting gas in the range of $\log(n_{\text{H}}/\text{cm}^{-3}) = 0 - 1$ (Table 1) provides a further differentiating factor and indicates that feedback shocks are the likely dominant powering source for the collisional excitation generated $\text{Ly}\alpha$ emission in LABs. The small locus at density of $\sim 10^{-3} \text{ cm}^{-3}$ and temperature of $\sim 10^4 \text{ K}$ in the top left panel of Figure 5 is due to photoionization produced $\text{Ly}\alpha$ emission (via recombination), the other primary power source. The photoionization seems to be only on halo-scales as seen in Figure 3. The separation of the collisionally powered and photoionization powered for the $\text{Ly}\alpha$ line is easily visible in the bottom-left panel of Figure 5.

Both He II and C IV emission each have a minor photoionization component, seen as the loci at hydrogen density of $\sim 10^{-3} \text{ cm}^{-3}$ and temperature of $\sim 10^{4-5} \text{ K}$ in the top middle and bottom right panels. In stark contrast to the $\text{Ly}\alpha$ line, the photoionization powered emission for He II and C IV lines is much weaker, seen in the lack of significant emission peaks at the low density end ($\sim 10^{-3} - 10^{-2} \text{ cm}^{-3}$) in the red dashed and blue dotted curves in the bottom-left panel of Figure 5. Note that the temperature of $\log T \sim 5$ is the temperature for maximum abundance of C IV by collisional processes and thus is consistent with collision excitation being the responsible process for C IV emission. Indeed, this conclusion is reached by [Arrighi Battaia et al. \(2015a\)](#) and [Arrighi Battaia et al. \(2015b\)](#); the high sensitivity of this line to temperature is noted in [Groves et al. \(2004\)](#). This is also consistent with the fact that the concerned C IV emission line is a resonant line as well. Most of the He II emission origi-

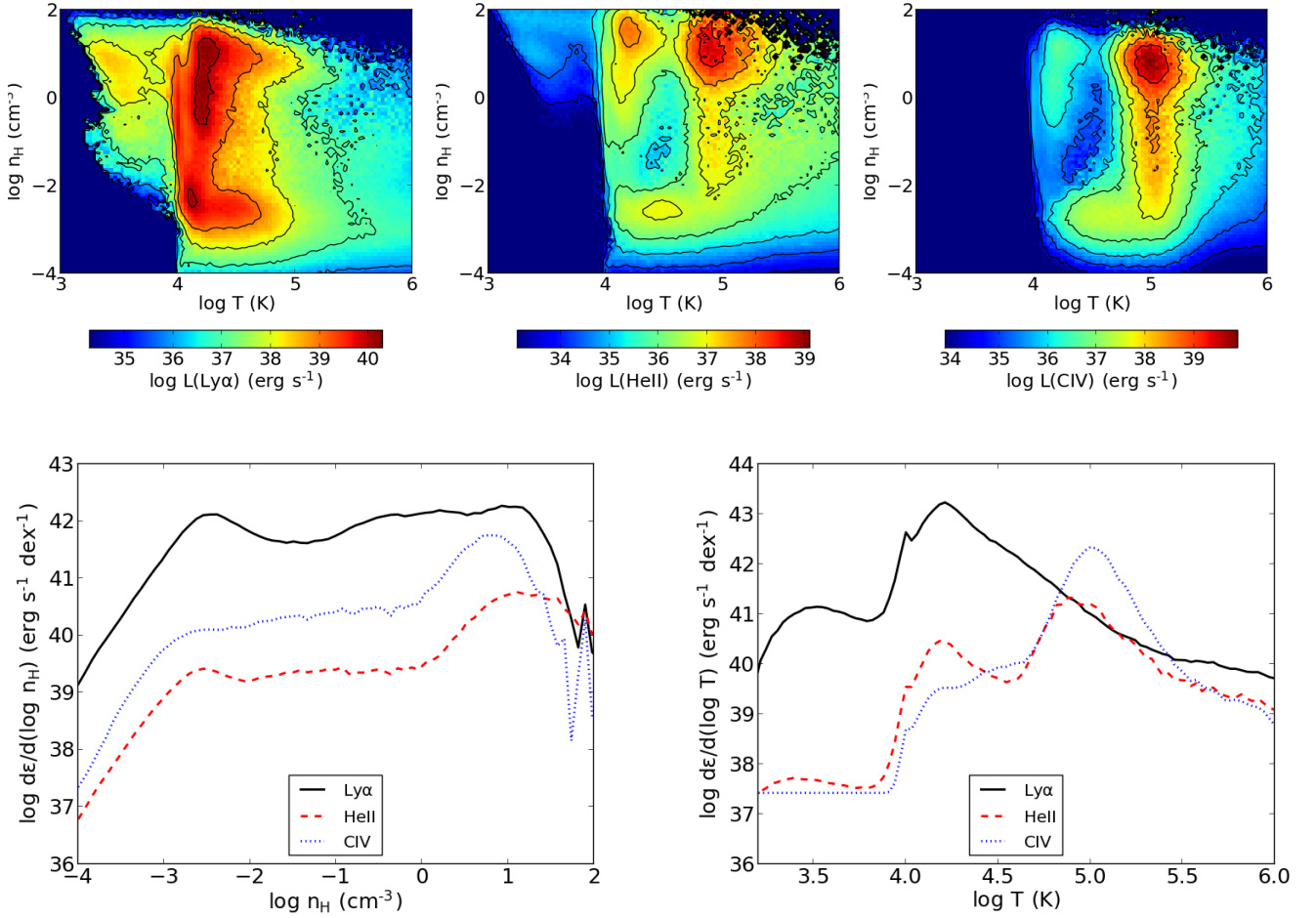


Figure 5. Top row: emission of each of the three lines (left panel for Ly α , middle panel for He II and right panel for C IV) in the temperature-density phase diagram. Bottom row: the distribution of each emission line in density (left panel) and temperature (right panel) for the Ly α , He II and C IV lines shown in black solid, red dashed and blue dotted curves, respectively, averaged over the 40 galaxies.

nates from regions of similar temperature ($\log T \sim 5$) as the C IV emission, but somewhat more dense ($n_H = 5 - 20 \text{ cm}^{-3}$). It is noted that at $\log T = 5$ the dominant ionization state of helium is He III. Thus, the dominant emission process for He II line is recombination via collisional ionization of He II. This is consistent with the He II 1640Å line is in analogy to hydrogen H α line).

To better understand the variations and commonalities between galaxies with respect to the emission of the three lines concerned, we list in Table 1 the emission-weighted metallicity, density and temperature for the three lines for the 40 simulated galaxies analyzed. We see that the metallicity ranges from 0.28 to $1.77 Z_\odot$. There is no universal trend of the metallicity with respect to the three lines, although in a typical case the mean metallicity increase from Ly α to C IV significantly and then to He II slightly. The typical range of (Ly α , C IV, He II) emission weighted metallicities are $(0.5 \pm 0.2, 1.0 \pm 0.2, 1.1 \pm 0.3) Z_\odot$. This is likely due to metal enrichment and mixing in the CGM (Shen et al. 2010; Crain et al. 2013; Brook et al. 2014; Ford et al. 2016), which is accounted for in our simulation by following metal transport

in a spatially resolved fashion at the high resolution of the AMR grid.

It is found that in most cases the Ly α emission-weighted gas density is in the range of $0.5 - 3 \text{ cm}^{-3}$, comparable to but slightly lower than $2 - 5 \text{ cm}^{-3}$ for C IV, which in turn is slightly lower than $5 - 20 \text{ cm}^{-3}$ for He II. It should be noted that this general trend does not hold on an individual basis, neither is there a definitive correlation between stellar mass of the galaxy and the emission-weighted gas density. This is indicative of and consistent with the notion that the gas density, the gas that bears the physical characteristics for strong line emission for three lines concerned in particular, fluctuates in time. This bodes well with the notion that star formation, which is fueled by gas accretion, may fluctuate strongly and hence bursty in nature. Finally, the emission-weighted temperatures of the three lines differ significantly with that of Ly α slightly above 10^4 K , that of both C IV and He II about 10^5 K . The emission-weighted temperatures of the C IV line is very close to that of the He II line, visible in the red dashed and blue dotted curves in the bottom-right panel of Figure 5, although the He II line has a more pronounced photoionization peak at $T \sim 10^{4.2} \text{ K}$. Taking into

account the differences in metallicity, temperature and density of gas emitting the three emission lines, it is clear that, while there may be some overlaps, especially between He II and C IV lines, the zero-order picture emerging is that the three lines largely originate from different gas regions in a multi-phase interstellar and circumgalactic medium that is shock-heated primarily by stellar feedback/supernovae and secondarily by gravitational energy of accreting gas. Figure 6 demonstrates this finding through emission weighted maps of one of the galaxies in our sample. The emission regions trace different gas properties (temperature, density and metallicity) with some degree of overlap.

While our model appears to have the ability to account for the observed line ratios of He II /Ly α and C IV /Ly α , based on a model that has provided the first successful explanation for Ly α emission properties (size-luminosity relation and luminosity function) of observed LABs, it is useful to bear in mind that there is still significant freedom available to us for adjustments of the two parameters, β and γ in Eq 1, largely due to our inability to precisely constrain simultaneously the distributions of gas density, temperature and metallicity, upon which dust formation and hence the obscuration/absorption sensitively depends, among others. This ambiguity may be somewhat mitigated by the fact that the number of parameters in our modeling is outnumbered by the number of observational constraints. Nevertheless, we plan to investigate other diagnostic emission and absorption lines to further test the consistency of our model.

5 DISCUSSION AND CONCLUSIONS

Utilizing *ab initio* ultra-high resolution (LAOZI) hydrodynamical simulations, we have previously shown that the observed size-luminosity and luminosity function of LABs can be successfully reproduced, with the extended Ly α 1216Å emission powered by a combination of central star formation and central shock heated gas (Cen & Zheng 2013). In this study, we investigate two additional emission lines of LABs: He II 1640Å and C IV 1549Å. Two parameters are introduced and adjusted for modeling the dust attenuation. With that, we show that our simulations can reproduce simultaneously the observed C IV /Ly α and He II /Ly α ratios, in addition to the agreements for the LAB luminosity function, luminosity-size relation that have been achieved before.

We show that the He II 1640Å and C IV 1549Å are largely powered by shocked heated gas, due primarily to feedback shocks from supernovae and secondarily to gravitational gas accretion shocks. The C IV emission line is primarily collisional excitation driven, while the He II emission line is powered mainly by collisional ionization, with in situ photoexcitation/photoionization being a minor contributor for either of the lines. The Ly α emission line is powered by a combination of stellar radiation and collisional excitation, both being significantly more centrally concentrated than the observed Ly α emission surface brightness profile; we have shown in Cen & Zheng (2013) that resonant scattering and spatial diffusion of Ly α photons produce the extended, diffuse emission observed, in conjunction with clustering of galaxies. Cen & Zheng (2013) also show that the peak of the Ly α emission need not originate from a compact source

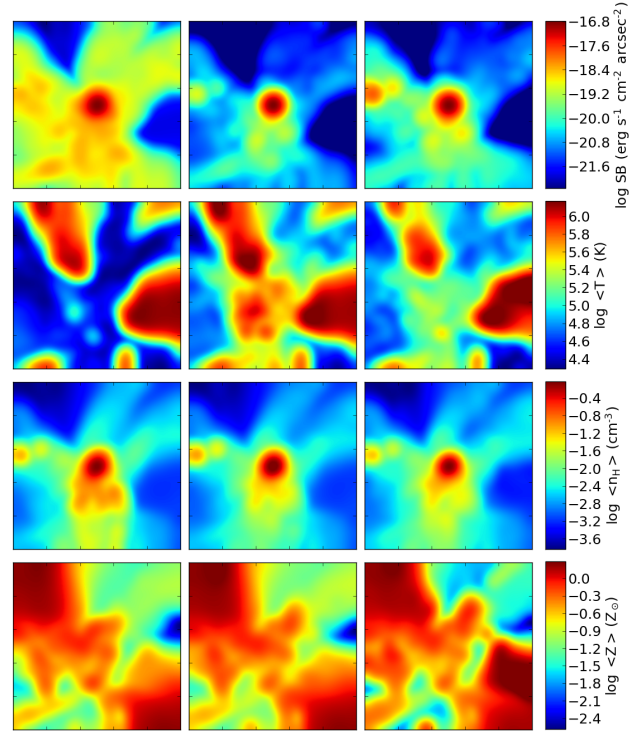


Figure 6. Projection plots (100 kpc x 100 kpc) for a randomly selected galaxy (ID 5). From left to right, emission lines Ly α , He II, and C IV. From top to bottom, surface brightness, and emission weighted temperature, density, and metallicity. Distinct emission regions for each of the three lines are visible, and are characteristic of different combinations of properties.

via detailed radiative transfer methods, consistent with the findings of Prescott et al. (2012) and Prescott et al. (2015).

We find that the density, temperature and metallicity of the gas responsible for each emission line is significantly distinct, in a multi-phase interstellar and circumgalactic medium. We see in Figure 5 that most of the Ly α emission originates from the collisionally excited gas with $\log(n_H/\text{cm}^{-3}) = 0 - 1$, temperature $\log(T/\text{K}) \sim 4.2$ and sub-solar metallicity. Most of the He II emission originates from regions of temperature of $\log T \sim 5$, density of $n_H = 5 - 20 \text{ cm}^{-3}$ and solar metallicity. Overall, the physical properties of the C IV emitting gas is similar to those of the He II emitting gas. On an individual galaxy basis, however, the mean emission-weighted gas densities, temperatures and metallicities for C IV and He II lines differ substantially, indicative of significantly differing, albeit overlapping, emission regions.

We have used the very useful and versatile analysis software yt version 2.6 (Turk et al. 2011) for some of our analysis. Computing resources were in part provided by the NASA High- End Computing (HEC) Program through the NASA Advanced Supercomputing (NAS) Division at Ames Research Center. The research is supported in part by NASA grant NNX11AI23G, NASA grant NNX14AC89G and NSF grant AST-1208891.

REFERENCES

Arrigoni Battaia F., Yang Y., Hennawi J. F., Prochaska J. X.,

- Matsuda Y., Yamada T., Hayashino T., 2015a, *ApJ*, **804**, 26
- Arrigoni Battaia F., Hennawi J. F., Prochaska J. X., Cantalupo S., 2015b, *ApJ*, **809**, 163
- Brook C. B., Stinson G., Gibson B. K., Shen S., Macciò A. V., Obreja A., Wadsley J., Quinn T., 2014, *MNRAS*, **443**, 3809
- Bryan G. L., et al., 2014, *ApJS*, **211**, 19
- Cantalupo S., Arrigoni-Battaia F., Prochaska J. X., Hennawi J. F., Madau P., 2014, *Nature*, **506**, 63
- Cen R., 2012a, *ApJ*, **748**, 121
- Cen R., 2012b, *ApJ*, **753**, 17
- Cen R., 2014, *ApJ*, **781**, 38
- Cen R., Ostriker J. P., 1992, *ApJ*, **399**, L113
- Cen R., Zheng Z., 2013, *ApJ*, **775**, 112
- Cen R., Nagamine K., Ostriker J. P., 2005, *ApJ*, **635**, 86
- Crain R. A., McCarthy I. G., Schaye J., Theuns T., Frenk C. S., 2013, *MNRAS*, **432**, 3005
- Dey A., et al., 2005, *ApJ*, **629**, 654
- Draine B. T., 2003, *ARA&A*, **41**, 241
- Ferland G. J., et al., 2013, *Rev. Mex. Astron. Astrofis.*, **49**, 137
- Ford A. B., et al., 2016, *MNRAS*, **459**, 1745
- Groves B. A., Dopita M. A., Sutherland R. S., 2004, *ApJS*, **153**, 75
- Haardt F., Madau P., 2012, *ApJ*, **746**, 125
- Heckman T. M., Miley G. K., Lehnert M. D., van Breugel W., 1991a, *ApJ*, **370**, 78
- Heckman T. M., Lehnert M. D., Miley G. K., van Breugel W., 1991b, *ApJ*, **381**, 373
- Keel W. C., Cohen S. H., Windhorst R. A., Waddington I., 1999, *AJ*, **118**, 2547
- Komatsu E., et al., 2011, *ApJS*, **192**, 18
- Lake E., Zheng Z., Cen R., Sadoun R., Momose R., Ouchi M., 2015, *ApJ*, **806**, 46
- Matsuda Y., et al., 2004, *AJ*, **128**, 569
- Matsuda Y., et al., 2011, *MNRAS*, **410**, L13
- McLinden E. M., Malhotra S., Rhoads J. E., Hibon P., Weijmans A.-M., Tilvi V., 2013, *ApJ*, **767**, 48
- Mori M., Umemura M., 2006, *New Astron. Rev.*, **50**, 199
- Peeples M. S., Werk J. K., Tumlinson J., Oppenheimer B. D., Prochaska J. X., Katz N., Weinberg D. H., 2014, *ApJ*, **786**, 54
- Prescott M. K. M., Dey A., Jannuzi B. T., 2009, *ApJ*, **702**, 554
- Prescott M. K. M., et al., 2012, *ApJ*, **752**, 86
- Prescott M. K. M., Dey A., Jannuzi B. T., 2013, *ApJ*, **762**, 38
- Prescott M. K. M., Momcheva I., Brammer G. B., Fynbo J. P. U., Møller P., 2015, *ApJ*, **802**, 32
- Shen S., Wadsley J., Stinson G., 2010, *MNRAS*, **407**, 1581
- Steidel C. C., Adelberger K. L., Shapley A. E., Pettini M., Dickinson M., Giavalisco M., 2000, *ApJ*, **532**, 170
- Taniguchi Y., Shioya Y., 2000, *ApJ*, **532**, L13
- Turk M. J., Smith B. D., Oishi J. S., Skory S., Skillman S. W., Abel T., Norman M. L., 2011, *ApJS*, **192**, 9
- Yang Y., Zabludoff A., Eisenstein D., Davé R., 2010, *ApJ*, **719**, 1654
- Yang Y., Zabludoff A., Jahnke K., Eisenstein D., Davé R., Shectman S. A., Kelson D. D., 2011, *ApJ*, **735**, 87
- Yang Y., Zabludoff A., Jahnke K., Davé R., 2014, *ApJ*, **793**, 114
- Zheng Z., Wallace J., 2014, *ApJ*, **794**, 116
- Zheng Z., Cen R., Trac H., Miralda-Escudé J., 2010, *ApJ*, **716**, 574